

Impact of a non-Gaussian density field on Sunyaev-Zeldovich observables

Sharon Sadeh^{1*}, Yoel Rephaeli^{1,2} and Joseph Silk³

¹*School of Physics and Astronomy, Tel Aviv University, Tel Aviv, 69978, Israel*

²*Center for Astrophysics and Space Sciences, University of California, San Diego, La Jolla, CA 92093-0424*

³*Department of Astrophysics, University of Oxford, Keble Road, OX1 3RH, UK*

27 October 2018

ABSTRACT

The main statistical properties of the Sunyaev-Zeldovich (S-Z) effect - the power spectrum, cluster number counts, and angular correlation function - are calculated and compared within the framework of two density fields which differ in their predictions of the cluster mass function at high redshifts. We do so for the usual Press & Schechter mass function, which is derived on the basis of a Gaussian density fluctuation field, and for a mass function based on a χ^2 distributed density field. These three S-Z observables are found to be very significantly dependent on the choice of the mass function. The different predictions of the Gaussian and non-Gaussian density fields are probed in detail by investigating the behaviour of the three S-Z observables in terms of cluster mass and redshift. The formation time distribution of clusters is also demonstrated to be sensitive to the underlying mass function. A semi-quantitative assessment is given of its impact on the concentration parameter and the temperature of intracluster gas.

Key words: galaxies:clusters:general – cosmic microwave background – large-scale structure of the Universe

1 INTRODUCTION

It has recently been suggested that several observational results may be hinting at a significant non-Gaussian component in the primordial density fluctuation field (Mathis, Diego, & Silk 2004, hereafter MDS). Among these are the detection of structures with high velocity dispersions at redshifts $z = 4.1$ (Miley et al. 2004) and $z = 2.1$ (Kurk et al. 2004), the apparent slow evolution of the X-ray cluster luminosity function indicated by objects taken from the Vikhlinin et al. (1998) and Mullis et al. (2003) cluster catalogs, and the enhancement of the CMB power spectrum at high multipoles that was measured by the *CBI* (Mason et al. 2003) and *ACBAR* (Kuo et al. 2004) experiments. MDS pointed out that scale-dependent non-Gaussianity may be probed through its detectable manifestations on the large mass scales of clusters of galaxies, and that this is possible without necessarily violating constraints on non-Gaussianity such as those obtained from *WMAP* all-sky CMB maps (Komatsu et al. 2003). It is argued by MDS that while it is hard (although possible) to reconcile the observational results with predictions made on the basis of a Gaussian field, these arise more naturally with either positively-or negatively-skewed density fields.

In this paper we extend the work of MDS, focusing on the impact of a positively-skewed non-Gaussian field on the principal statistical properties of the Sunyaev-Zeldovich (S-Z) effect. We compare in detail the predicted S-Z power spectrum, cluster number counts, and the angular correlation function for Gaussian and non-Gaussian models.

In section 2 we specify the various models and scalings used in order to carry out the calculations; specifically, a complete account of the mass functions and the relevant scalings for the quantification of cluster-induced Comptonization are provided. Results of the calculations relating to the S-Z power spectrum and number counts are detailed in section 3. In section 4 we formulate the method of calculation of the 2-point angular correlation function of S-Z clusters and present the corresponding results. The calculation of cluster formation times within the framework of non-Gaussian fields requires a slight modification of the corresponding Gaussian case. This is explained in section 5. Results of the formation time computations in both the

* E-mail: shrs@post.tau.ac.il

Gaussian and non-Gaussian models follow in the same section, followed by a brief discussion and a summary of our main conclusions in section 6.

2 THE MODEL

Calculations of statistical properties of the evolving cluster population involve the basic cosmological and large-scale quantities and parameters, as well as essential properties of intracluster (IC) gas. Detailed description of the calculation of integrated S-Z properties can be found in the literature. Therefore, our brief treatment here highlights only those aspects that pertain to the basic properties of the density fields explored in this work. The multiplicity function in the Press & Schechter (1974) formalism is

$$n(M, z) = -F(\mu) \frac{\rho_b}{M\sigma} \frac{d\sigma}{dM} dM, \quad (1)$$

where $\mu \equiv \delta_c/\sigma$ and ρ_b is the background density. The critical overdensity for spherical collapse is assumed to be constant, $\delta_c = 1.69$, owing to its weak dependence on redshift. The density field variance, smoothed over a top-hat window function of radius R , is calculated through

$$\sigma^2(R) = \int_0^\infty P(k) \widetilde{W}^2(kR) k^2 dk, \quad (2)$$

where $P(k) \equiv Ak^n T^2(k)$. The mass variance evolves with redshift according to

$$\sigma(M, z) = \frac{\sigma(M, 0) g[\Omega_m(z)]}{1+z g[\Omega_m(0)]}, \quad (3)$$

where

$$\Omega_m(z) = \frac{\Omega_m(0)(1+z)^3}{(1+z)^2[1 + \Omega_m(0)z - \Omega_\Lambda(0)]}; \quad \Omega_\Lambda(z) = 1 - \Omega_m(z), \quad (4)$$

and (Carroll, Press & Turner 1992)

$$g[\Omega_m(z)] = \frac{2.5\Omega_m(z)}{[\Omega_m(z)^{4/7} - \Omega_\Lambda + (1 + \Omega_m(z)/2)(1 + \Omega_\Lambda/70)]}. \quad (5)$$

The function $F(\mu)$ in equation (1) assumes the form

$$F(\mu) = \sqrt{\frac{2}{\pi}} e^{-\frac{\mu^2}{2}} \frac{\mu}{\sigma_R}, \quad (6)$$

for a Gaussian density field, and the form

$$F(\mu) = \frac{\left(1 + \sqrt{\frac{2}{m}}\mu\right)^{m/2-1}}{\left(\frac{2}{m}\right)^{(m-1)/2} \Gamma\left(\frac{m}{2}\right)} e^{-\frac{m}{2}\left(1 + \sqrt{\frac{m}{2}}\mu\right)} \frac{\mu}{\sigma_R}, \quad (7)$$

for a density fluctuation field which is distributed according to the χ_m^2 model (Koyama, Soda & Taruya 1999). The parameter m describes the number of CDM fields added in quadratures, so as to yield the requested distribution.

In most of our calculations we use $m = 1$, which constitutes the largest possible deviation from a normally distributed probability density function (PDF) for this model. Increasing the number of random density fields obviously results in a PDF that approaches a Gaussian, in accordance with the central limit theorem. Some of the calculations were done also for the case $m = 2$ in order to illustrate the impact of this parameter on the high-mass tail of the PDF. The respective mass functions are then obtained by multiplying either expression by a common factor, as explicitly stated in equation (1).

For the Gaussian case an adiabatic CDM transfer function is employed,

$$T(k)_{CDM} = \frac{\ln(1 + 2.34q)}{2.34q} [1 + 3.89q + (16.1q)^2 + (5.46q)^3 + (6.71q)^4]^{-1/4}, \quad (8)$$

whereas an isocurvature CDM transfer function is chosen for the χ_m^2 model,

$$T(k)_{CDM, isoc} = (5.6q)^2 \left[1 + \frac{(40q)^2}{1 + 215q + (16q)^2(1 + 0.5q)^{-1}} + (5.6q)^{8/5} \right]^{-5/4}, \quad (9)$$

with $q \equiv k/(\Omega_m h^2) Mpc^{-1}$. Both transfer functions were taken from Bardeen et al. (1986). The calculations were carried out for a Λ CDM model, with $\Omega_\Lambda = 0.7$, $\Omega_m = 0.3$, $h = 0.7$. In the Gaussian case the spectral index was taken to be $n = 1$ and the normalization $\sigma_8 = 0.9$. In the non-Gaussian case $n = -1.8$, and from the requirement that the present cluster abundance is the same as calculated in the Gaussian model, we obtain $\sigma_8 = 0.73$.

The S-Z angular power spectrum is calculated using the basic expression

$$C_\ell = \int_z r^2 \frac{dr}{dz} \int_M n(M, z) G_\ell(M, z) dM dz, \quad (10)$$

where r is the co-moving radial distance, and G_ℓ is obtained from the angular Fourier transform of the profile of the temperature change induced by Comptonization of the CMB at an angular distance θ from the centre of a cluster, $\Delta T(\theta)$. The function G_ℓ , which is proportional to $\Delta T(\theta)^2$, is fully specified in, e.g., Molnar & Birkinshaw (2000). In the limit of non-relativistic electron velocities (more on this in section 3.2) the relative temperature change assumes the simple form

$$\frac{\Delta T}{T}(\theta) = \left[x \coth\left(\frac{x}{2}\right) - 4 \right] y(\theta), \quad (11)$$

where, for an isothermal cluster with a β density profile, the Comptonization parameter is

$$y(\theta) = 2 \frac{k_B \sigma_T}{m_e c^2} \frac{n_0(M, z) T_0(M, z) r_c(M, z)}{\sqrt{1 + (\theta/\theta_c)^2}} \tan^{-1} \left[p \sqrt{\frac{1 - (\theta/p\theta_c)^2}{1 + (\theta/\theta_c)^2}} \right]. \quad (12)$$

Here n_0 , T_0 , r_c , and θ_c denote the central electron density, temperature, core radius, and the angle subtended by the core, respectively. The virial radius is taken throughout to be $p = 10$ times r_c .

Of crucial importance are the scalings of cluster properties with mass and redshift; the temperature is assumed to scale as

$$T(M, z) = T_{15} \left(\frac{M}{10^{15} h^{-1} M_\odot} \right)^\alpha (1+z)^\psi, \quad (13)$$

where a temperature of 8.5 keV is ascribed to a cluster with mass $10^{15} h^{-1} M_\odot$ at present. The parameter α is usually taken to be $2/3$, in accordance with theoretical predictions based on hydrostatic equilibrium. We allow a variance of 10% in its value, as to possibly address non-gravitational effects which may result in a deviation from the simplistic assumption of hydrostatic equilibrium, and also to reflect the observed variance in this parameter. An additional uncertainty relating to this scaling is represented in the parameter ψ , which describes the temporal evolution of cluster temperatures, and is taken to be either zero or unity, constituting two limiting cases for which there is either no evolution, or strong evolution, respectively. Little is known on the evolution of the X-ray temperature function due to the lack of X-ray observations of high-redshift clusters, although some interesting insight is gained from hydrodynamical simulations (Norman 2005).

The electron density is parameterized as

$$n_e(M, z) \simeq n_0 \frac{f}{0.1} (1+z)^3, \quad (14)$$

with the scaling of the gas mass fraction to $\sim 10\%$ (e.g., Carlstrom, Holder & Reese 2002). Since we do not yet know the redshift dependence of f , we assume $f = 0.1$ to be roughly valid throughout the redshift considered here. Finally, the core radius is calibrated according to the simple relation

$$r_c = 0.15 h^{-1} \left(\frac{M}{10^{15} h^{-1} M_\odot} \right)^{1/3} \frac{1}{1+z} \text{ Mpc}. \quad (15)$$

In accord with observational results, we adopt a variance of 20% in the value of the core radius. In order for the mass to remain constant when different scalings are used for the core radius, a corresponding change is affected in the central gas density.

The number of clusters with S-Z flux (change) above $\Delta \bar{F}_\nu$ is (e.g. Colafrancesco et al. 1997)

$$N(> \Delta \bar{F}_\nu) = \int r^2 \frac{dr}{dz} dz \int_{\Delta \bar{F}_\nu} n(M, z) dM. \quad (16)$$

For a cluster with mass M at redshift z

$$\Delta F_\nu = \frac{2(k_b T)^3}{(hc)^2} g(x) y_0 \int R_s (|\hat{\gamma} - \hat{\gamma}_\ell|, \sigma_B) \cdot y(|\hat{\gamma}_\ell|, M, z) d\Omega, \quad (17)$$

where $\hat{\gamma}_\ell$ and $\hat{\gamma}$ denote line of sight (los) directions through the cluster centre, and relative to this central los, respectively,

$$y_0 = 2 \frac{k_b \sigma_T}{m_e c^2} n_0(M, z) T_0(M, z) r_c(M, z), \quad (18)$$

and the spectral dependence (of the thermal component) of the effect is given (in the nonrelativistic limit; more on this in section 3.2) by

$$g(x) \equiv \frac{x^4 e^x}{(e^x - 1)^2} [x \coth(x/2) - 4], \quad (19)$$

where $x = h\nu/kT$. The profile of the effect is given in

$$y(|\hat{\gamma}_\ell|, M, z) \equiv \frac{1}{\sqrt{1 + (\theta/\theta_c)^2}} \cdot \tan^{-1} \left[p \sqrt{\frac{1 - (\theta/p\theta_c)^2}{1 + (\theta/\theta_c)^2}} \right], \quad (20)$$

which is the los integral along a direction that forms an angle θ with the cluster centre. $R_s(|\hat{\gamma} - \hat{\gamma}_\ell|, \sigma_B)$ denotes the angular response of a detector whose beam size is given in terms of σ_B . Finally,

$$\Delta \bar{F}_\nu = \frac{\int \Delta F_\nu E(\nu) d\nu}{\int E(\nu) d\nu}, \quad (21)$$

is the flux weighted over the detector spectral response $E(\nu)$.

Only clusters for which the S-Z flux exceeds the *PLANCK/HFI* detection limit of 30 mJy are considered here. This is manifested in the lower limit of the mass function integral, equation (16). The results for the S-Z power spectrum and number counts described below refer to these two models: (a) IC gas temperature evolves with time according to $\psi = 1$, and (b) no temperature evolution, $\psi = 0$. Power spectra were calculated at $\nu = 353 \text{ GHz}$, with a beam size is $7.1'$. Number counts were calculated also at $\nu = 143 \text{ GHz}$ and $\nu = 545 \text{ GHz}$.

3 RESULTS

3.1 Power spectrum

Several qualitative assessments can be pointed out before we describe specific results. The longer tail of the non-Gaussian distribution function (with respect to that of the Gaussian) at the high mass end translates to higher cluster abundance in general, and high mass clusters in particular. This holds in the entire redshift range (with the exception of $z = 0$, since the mass function in the non-Gaussian case was normalized such as to yield the same cluster abundance as in the Gaussian case). This tendency stems from the fact that a positively-skewed density fluctuation field exhibits earlier cluster formation by enhancing the probability that the average density within a spherical region of any size exceeds the critical density for collapse. Consequently, the S-Z power spectrum is expected to attain higher levels in the non-Gaussian case. Owing to the inferred denser population of clusters at high redshifts, the magnitude at the peak should shift to higher multipoles, reflecting the higher density of distant clusters with smaller angular sizes. Naturally, this effect would be drastically reduced in a non-evolving temperature scenario due to the inferred lower temperatures associated with high redshift clusters when the $(1+z)$ scaling is factored out.

The S-Z power spectrum calculated for cases (a) and (b) is plotted in Figs. 1 through 5 (with the exception of Fig. 3). In all plots the upper and lower panels correspond to cases (a) and (b), respectively, whereas the left- and right-hand panels pertain to the Gaussian and χ^2 models, respectively. Partial contributions to the total power spectrum from redshift intervals of $\Delta z = 1$ are shown in Fig. 1. Fig. 2 depicts partial contributions from (logarithmic) mass intervals of $\log \Delta M = 1$ to the total power spectrum. Power variation corresponding to a 10% variance in the parameter α , the scaling of cluster temperature with mass, is illustrated in Fig. 4. Finally, the impact of introducing a variance of 20% in the cluster core scaling on the magnitude of the S-Z power spectrum is shown in Fig. 5.

Referring first to the magnitude of the total power spectrum in Fig. 1, corresponding to the redshift interval $0 < z < 6$, in both cases (a) and model (b) higher levels of power are clearly evident in the non-Gaussian model. Quantitatively, the maximum power levels attained in case (a) are $\sim 3 \cdot 10^{-12}$ and $\sim 6 \cdot 10^{-11}$ for the Gaussian and non-Gaussian models, respectively. Note that both peak at multipoles higher than $\ell > 10,000$; in the Gaussian model this is due to the high gas densities of distant clusters implied by the constancy of the gas fraction, whereas in the non-Gaussian model the combination of high gas densities and the long tail at the high-mass cluster end is responsible for this result. Compared to case (a), distant clusters are cooler in case (b) by virtue of the redshift independence of their temperatures, resulting in lower power levels ($\sim 8^{-13}$ and $5 \cdot 10^{-12}$) in the Gaussian and χ^2 models, respectively. In the Gaussian model the power peaks at $\ell \sim 6000$, reflecting the lower contribution from cooler, more distant clusters. In the non-Gaussian model, a relatively high abundance of massive clusters at high redshifts (i.e. small angular scales) leads to sustained high power levels on these scales. It is also worth recalling that regardless of whether or not the temperature changes with redshift, it still increases with increasing mass, so even when $\psi = 0$ a denser population of hot clusters is produced in the long tail of the χ^2 PDF.

The contribution of clusters lying at relatively high redshifts to the overall power is clearly seen in the χ^2 model. In fact, in case (a) the contribution of clusters lying in the redshift range $0 < z < 1$ peaks at $\ell \sim 3000$. However, the total power continues to rise owing to the non-negligible power generated by clusters situated at $z > 1$, particularly so from redshift range $1 < z < 2$. In fact, at $\ell \sim 8000$ this contribution is surpassed by the next redshift range, $2 < z < 3$. In the Gaussian model the contribution from this range to the overall power is decidedly negligible. The same effect, although less pronounced, is evident in case (b); here distant clusters are cooler [than in the corresponding case (a)] by virtue of the $\psi = 0$ scaling. Consequently, the partial contributions from redshift ranges $1 < z < 3$ is still discernible, but to a lesser degree than in case (a).

Fig. 2 illustrates the distribution of S-Z power in four mass ranges. Most striking is the relative contribution to power

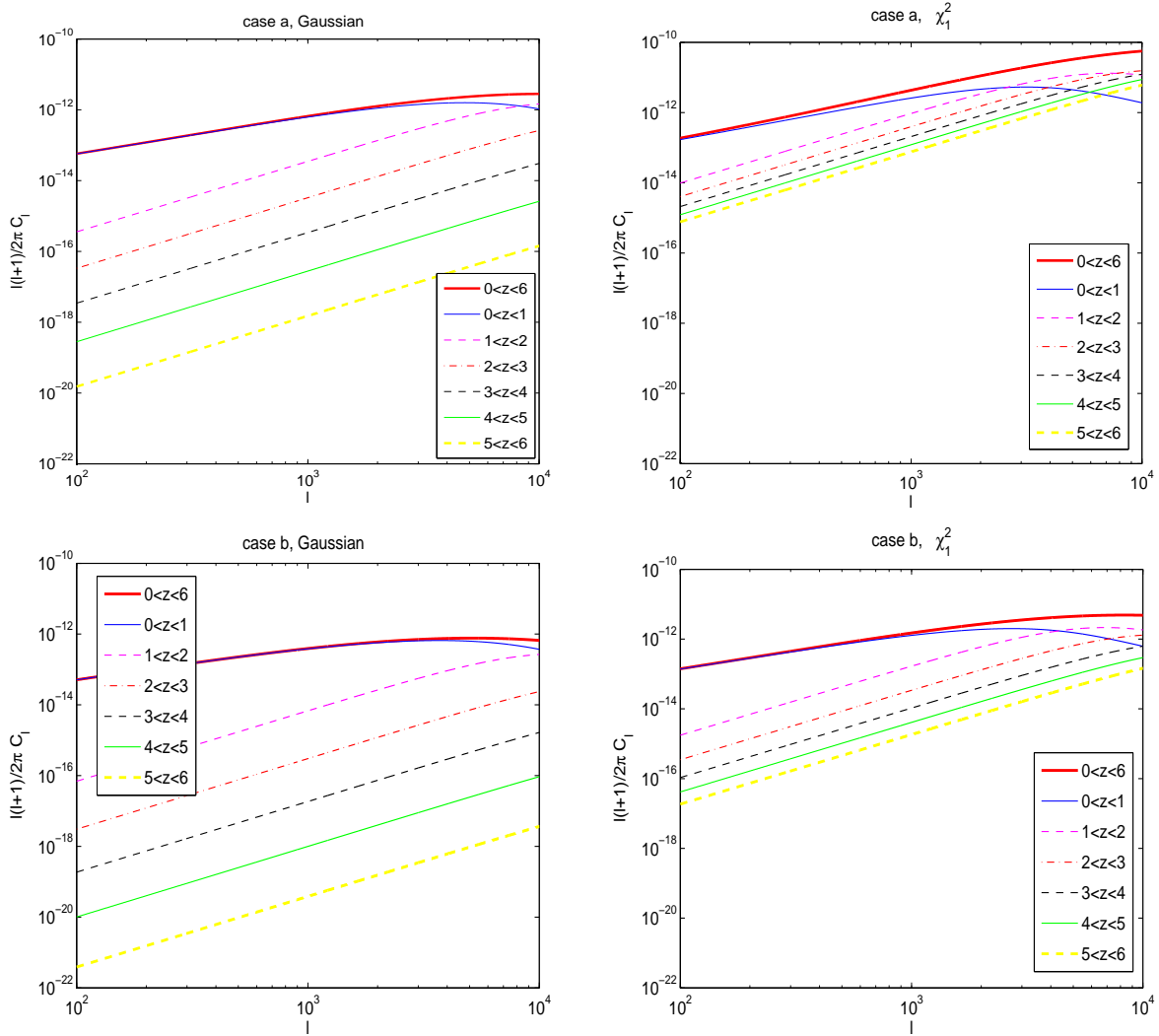


Figure 1. Angular power spectrum of the S-Z effect. Shown are levels of power contributed by clusters lying at redshift range of $0 < z < 6$, and at 6 redshift intervals. Left and right-hand panels correspond to the Gaussian and χ_1^2 models, respectively. Upper and lower panels relate to cases (a) and (b), respectively

from clusters lying in the $10^{15} h^{-1} M_\odot < M < 10^{16} h^{-1} M_\odot$ mass range. Whereas it is practically negligible at all multipoles in the Gaussian model, this is not the case in the non-Gaussian model; in fact, these massive clusters dominate the total power up to $\ell \sim 1000$ and $\ell \sim 2000$ in cases (a) and (b), respectively. At higher multipoles the $10^{14} h^{-1} M_\odot < M < 10^{15} h^{-1} M_\odot$ range dominates. In the Gaussian model low-mass clusters of $10^{13} h^{-1} M_\odot < M < 10^{14} h^{-1} M_\odot$ prevail only at the highest multipoles. These clusters are obviously the most abundant objects predicted by a mass function based on a primordial density fluctuation field of Gaussian nature, and - in light of their relative small sizes (and low temperatures) - thus must lie at a relative proximity to the observer; more distant clusters of similar masses would not produce sufficiently strong S-Z signal to be detected. Otherwise, in the Gaussian case, the lion's share of power originates in clusters in the mass range $10^{14} h^{-1} M_\odot < M < 10^{15} h^{-1} M_\odot$.

Fig. 1 and 2 explicitly demonstrate the significantly higher contribution of high-redshift - and therefore hotter, in particular in case (a) - clusters in the χ_1^2 model. This is manifested in higher power magnitude and at an intensification at higher multipoles corresponding to distant, low angular-size clusters. To further contrast the predictions of the two models, the ratio of total level of the S-Z power in the χ_1^2 model to that in the Gaussian model for cases (a) and (b) is shown in Fig. 3. For $\ell = 10^3 - 10^4$, this ratio increases from 7 to 20 in case (a), and from ~ 4 to ~ 7 in case (b).

The effect of changing α , the scaling of the cluster temperature with mass, is shown in Fig. 4. Since $T \propto (M/M_{15})^\alpha$, two different behaviours are expected for $M < M_{15}$ and $M > M_{15}$. For $M < M_{15}$, increasing α with respect to the conventional value of $2/3$ results in cooler clusters, whereas if $M > M_{15}$, higher temperatures will be attained. Lowering α results in the opposite effect, i.e., warmer low-mass clusters and cooler high-mass clusters. These changes affect the power spectrum for the

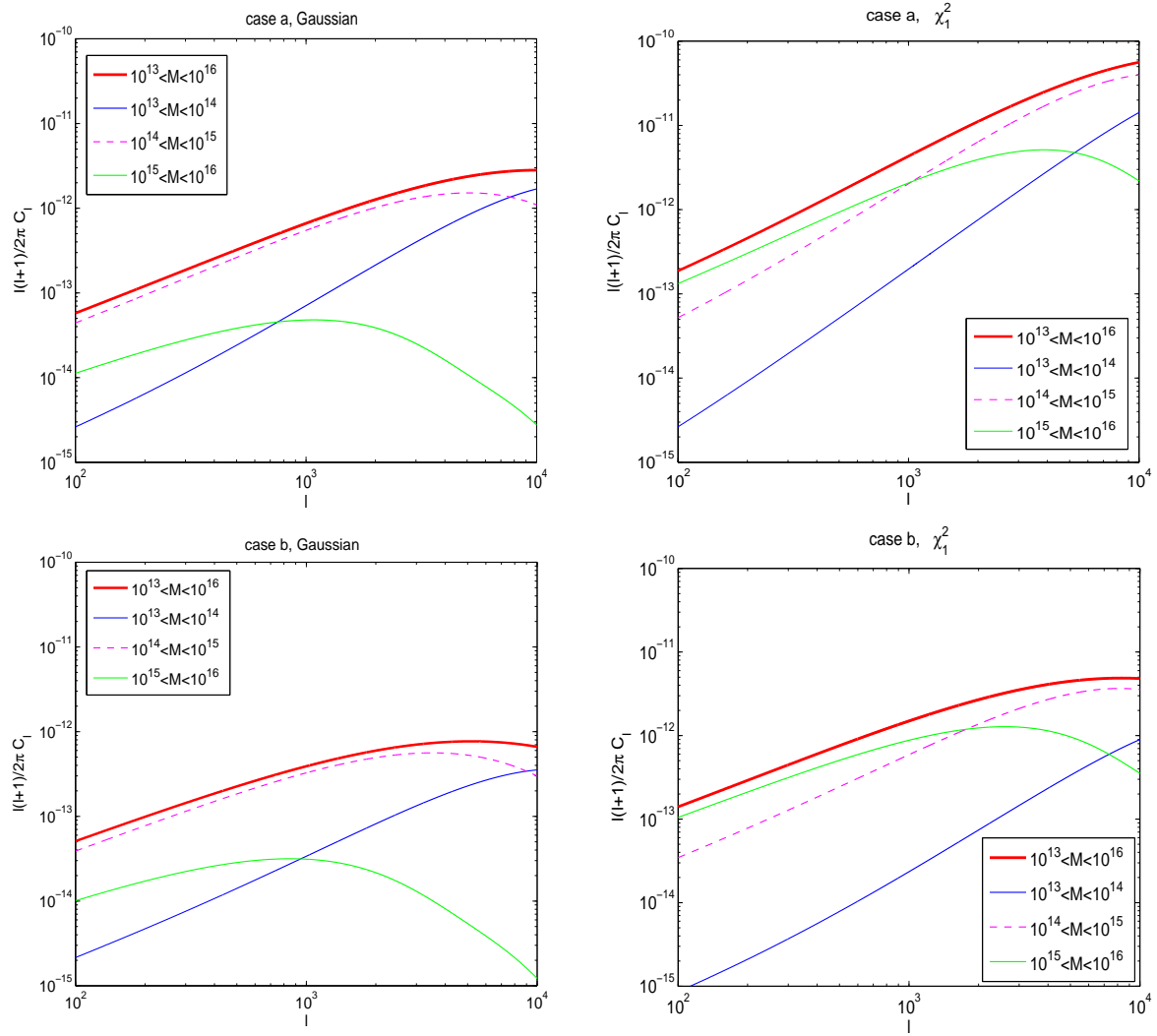


Figure 2. The same as in the previous figure, but here power spectrum levels are calculated for 4 mass intervals, spanning the range $10^{13}h^{-1}M_{\odot} < M < 10^{16}h^{-1}M_{\odot}$.

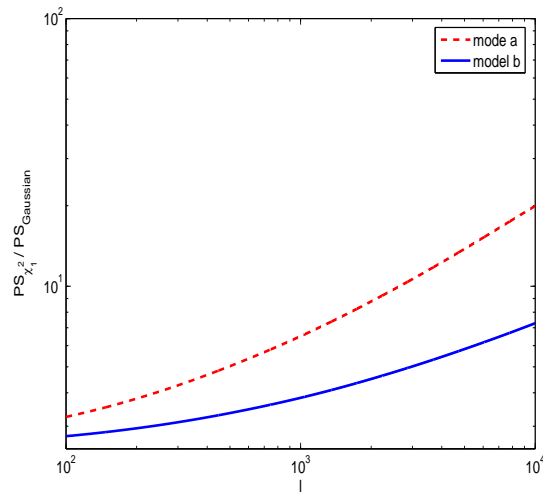


Figure 3. A comparison of S-Z power spectrum levels in the χ_1^2 and Gaussian models for cases (a) and (b).

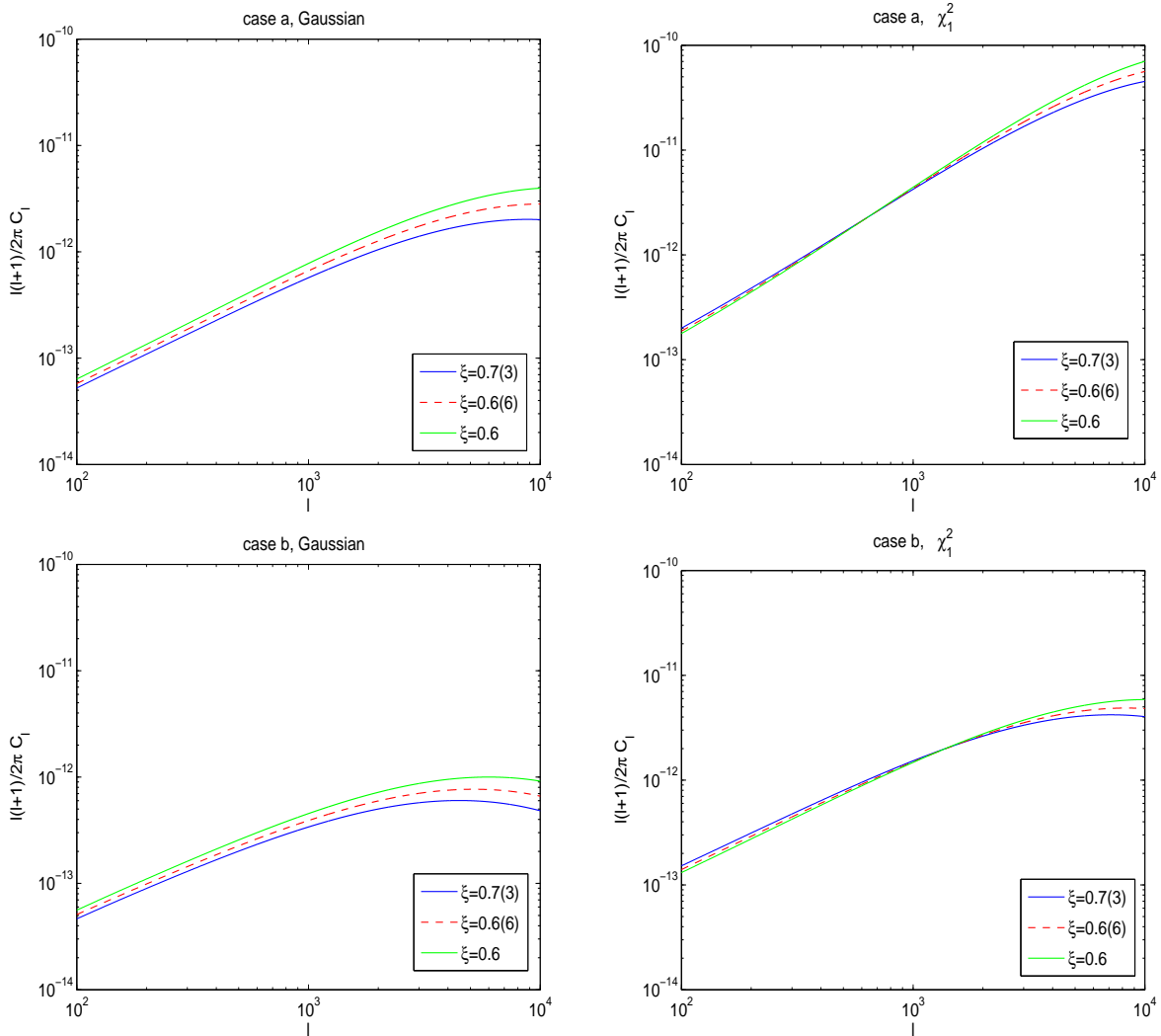


Figure 4. The impact of the temperature-mass relation on the S-Z power spectrum, $T \propto (M/M_{15})^\xi$. Shown are 3 cases: $\xi = 0.7(3)$, $\xi = 0.6(6)$, $\xi = 0.6$. The arrangement of the panels is the same as in the previous figures.

Gaussian and non-Gaussian models in slightly different ways; we have already seen that in the Gaussian model the largest contribution to the power spectrum comes from clusters with masses $10^{14} h^{-1} M_\odot < M < 10^{15} h^{-1} M_\odot$. That is, an outcome of increasing α is that most of the contributing clusters undergo cooling, and the level of power decreases. Obviously, lowering α has the opposite effect. This is clearly seen in the upper- and lower-left panels of Fig 4. It can also be seen (particularly so in the lower-left panel) that the curves peak at decreasing multipoles with increasing α . This has to do with the fact that the contribution of these relatively low-mass clusters to the overall power levels decreases with increasing α , so that power is suppressed from high multipoles, resulting in a leftward shift of the peaks. In the χ_1^2 model the results are somewhat different. Here the contribution to the power from high-mass clusters ($10^{15} h^{-1} M_\odot < M < 10^{16} h^{-1} M_\odot$) dominates at $\ell \lesssim 1000$ (case a) and $\ell \lesssim 2000$ (case b), whereas the corresponding contribution at higher multipoles originates in clusters lying within the mass range $10^{14} h^{-1} M_\odot < M < 10^{15} h^{-1} M_\odot$. In other words, an increment of power with increasing α is expected at lower multipoles, and a decrease of power with increasing α at higher multipoles. This is shown in the upper- and lower-right panels of Fig. 4.

We also investigate the influence of r_c on the power spectrum levels. The results are illustrated in Fig. 5, and are rather obvious. First, lowering or increasing the core radius changes the effective cluster size, and consequently, the multipole at which the power peaks. This can be easily seen in the lower-left panel of Fig. 5. In the remaining panels it is somewhat harder to notice the effect, owing to the fact that the peaks fall beyond $\ell = 10000$. Also, in order to keep the total gas mass constant, lower and higher core sizes necessitate higher and lower central gas densities, respectively. This results in higher and lower power levels for lower and higher core-sized clusters, respectively, as is apparent from the fact that the power spectrum scales as the central gas density squared (equations 10 and 12).

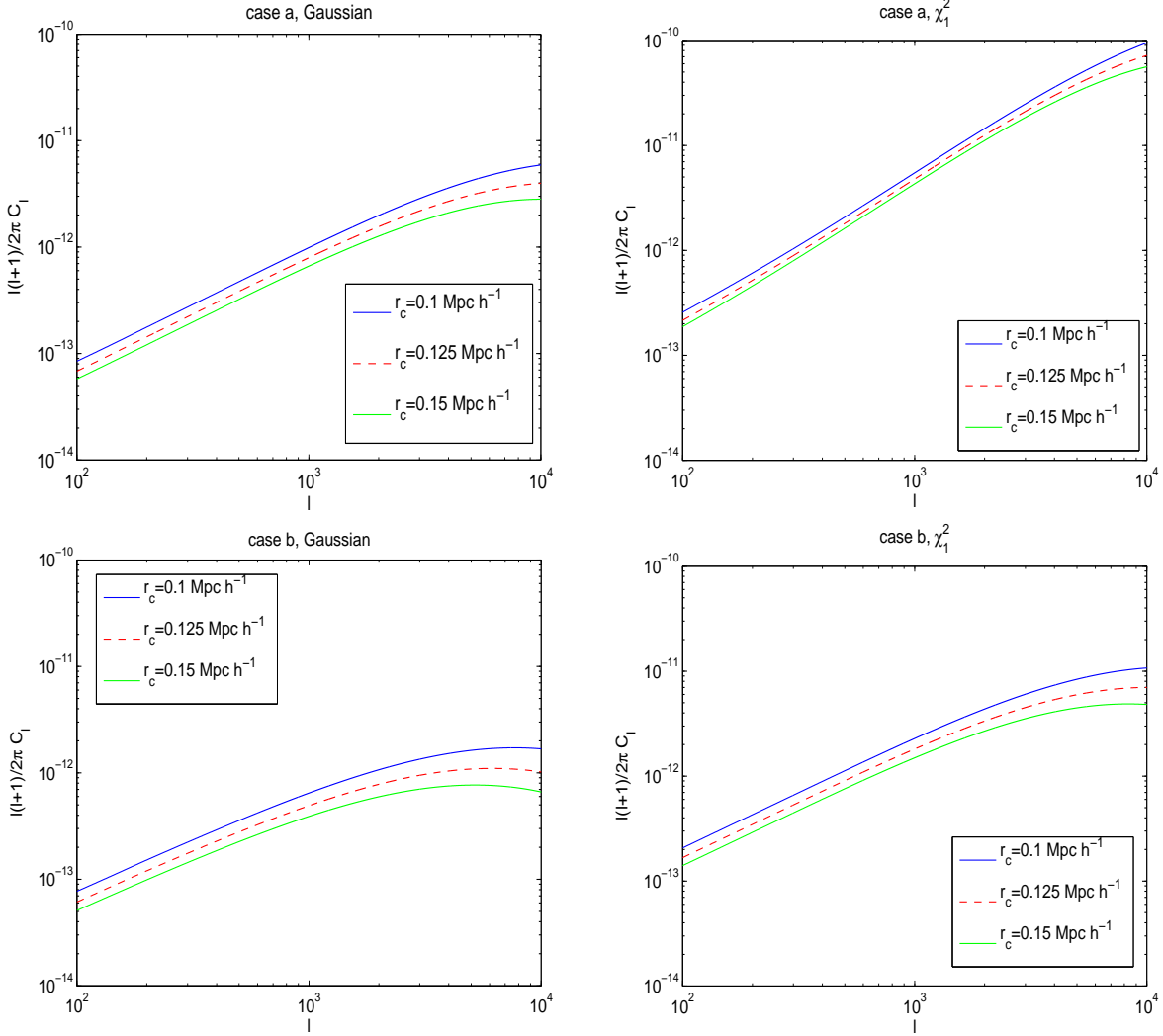


Figure 5. The impact of cluster core scaling on the S-Z power spectrum. Each of the three values considered ($r_c = 0.1, 0.125, 0.15 \text{ Mpc } h^{-1}$) denote the core radius of a cluster with mass $10^{15} M_{\odot} h^{-1}$ at redshift $z = 0$.

It is useful to mention some recent studies of S-Z power spectrum calculations and compare with our results. Case (a) of the Gaussian model is the most adequate for comparison, since past work has focused on Gaussian density fields, and whether analytically or inferred from hydrodynamical simulations, the IC gas temperature has been assumed (or observed) to increase with redshift (at least to a certain degree), in contrast with the constant temperature scenario, case (b). Da Silva et al. (2001) employed hydrodynamical simulations to find power levels of $5 - 9 \cdot 10^{12}$ peaking at $\ell \sim 7000$, depending on whether or not non-adiabatic processes such as preheating and radiative cooling were included. Their selection of cosmological parameters is essentially identical to ours, but the calculations were carried out in the Rayleigh-Jeans region, so a comparison between their results and ours requires an introduction of a multiplicative factor of 4 to our power levels. Consequently, the magnitude of the total power for case (a) in the Gaussian model peaks at multipole $\ell \sim 10,000$, at a value of $\sim 1.2 \cdot 10^{-11}$. Bond et al. (2005) have quantified the S-Z power spectrum using both analytic calculations and results of hydrodynamical simulations. The simulations yield peak power levels of $1 \sim 4 \cdot 10^{-11}$ at $\ell \sim 10,000$. Their analytic calculation yields similar power levels, but at lower peak multipoles, $\ell \sim 5000 - 6000$. Note that they calculated S-Z power at the *CBI* frequency, $\nu = 31 \text{ GHz}$. Rescaling our results to this frequency gives a power level of $\sim 1.1 \cdot 10^{-11}$. Refregier & Teyssier (2002) have also used hydrodynamical simulations and an analytic approach to calculate the S-Z power spectrum. They found that both methods yield approximately the same power levels (peaking at $\ell \sim 8000$ with magnitude $\gtrsim 10^{-11}$), particularly so when a cluster mass range $5 \cdot 10^{10} < M < 8 \cdot 10^{14} h^{-1} M_{\odot}$ is employed in the analytical calculation. The calculations were carried out in the R-J region. Springel, White & Hernquist (2001) employed hydrodynamical simulations, neglecting non-adiabatic processes, to infer power levels of $2 - 4 \cdot 10^{-11}$ at the peak, $\ell \sim 10,000$. In fact, the latter paper presents a detailed comparison of S-Z power spectra published in the literature showing a large scatter (spanning over an order of magnitude), which can

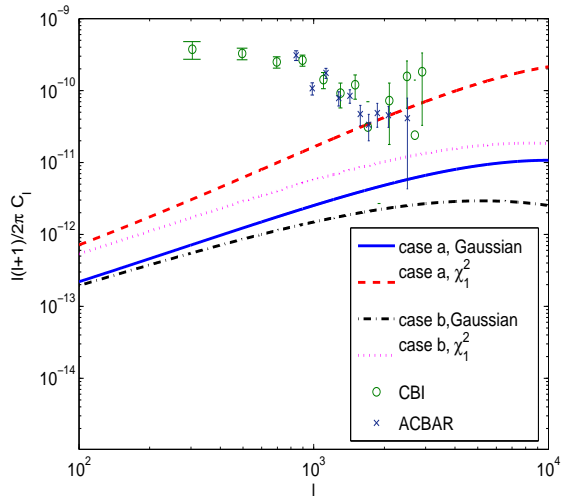


Figure 6. Total angular power spectrum of the S-Z effect as calculated above, together with results from the *CBI* and *ACBAR* experiments.

largely be attributed to uncertainties in the theoretical modeling of IC gas and the techniques implemented in hydrodynamical calculations. To complete this section, we combine, in a single plot, the total power spectrum levels of the S-Z effect in the Gaussian and χ_1^2 models, cases (a) and (b), with results from the *CBI* and *ACBAR* experiments. The analytic results were rescaled so as to correspond to an observation frequency of 31 GHz, corresponding to the *CBI* instrument. As can be seen in Fig. (6), it seems difficult to reconcile the Gaussian results with the data, whereas case (a) in the χ_1^2 model provides a reasonable match to the observed power excess at $l \gtrsim 2000$. These results agree with those found by Mathis et al. (2004).

3.2 Number counts

The qualitative considerations pertaining to the power spectrum that were presented in the previous section apply also to S-Z number counts: Higher (cumulative) counts are expected in the non-Gaussian case, and those are likely to be distributed differently in redshift space with respect to the Gaussian case, reflecting the higher population of massive clusters at high redshifts, which satisfy the detection flux limit. Fig. 7 depicts the redshift distribution of cumulative S-Z number counts. The arrangement of plots according to model is the same as in Fig. 1 through (5). In none of the models clusters with masses lower than $10^{14} h^{-1} M_\odot$ generate fluxes that exceed the adopted detection limit, $30 mJy$.

The most noticeable results displayed in the figure are: In the Gaussian model the largest contribution to the cumulative number counts (at $z = 0$) comes from clusters lying in the mass range $10^{14} h^{-1} M_\odot < M < 10^{15} h^{-1} M_\odot$. Actually, the cumulative number counts at $z = 0$ in this mass range are higher by at least an order of magnitude than those contributed by clusters in the mass range $10^{15} h^{-1} M_\odot < M < 10^{16} h^{-1} M_\odot$. Specifically, in case (a) the curves depicting the total counts and those contributed by clusters with masses in the range $10^{14} h^{-1} M_\odot < M < 10^{15} h^{-1} M_\odot$ are virtually identical. In case (b), however, at redshifts $z \gtrsim 0.5$ counts are dominated by clusters with higher masses, $10^{15} h^{-1} M_\odot < M < 10^{16} h^{-1} M_\odot$. This can be attributed to the fact that in case (b) the clusters in the former mass range have lower S-Z fluxes due to the lower temperatures as compared to clusters in case (a). Clusters belonging to the latter mass range are still massive enough (and consequently, hot enough) to compensate for the lack of temperature evolution. Regardless of this effect, it should be emphasized that the counts in the high mass range are negligible in comparison with the total cumulative counts at $z = 0$. A slightly different behaviour is apparent in case (a) of the χ_1^2 model; here total counts are still dominated by clusters in the mass range $10^{14} h^{-1} M_\odot < M < 10^{15} h^{-1} M_\odot$, although differences are not as pronounced as in the Gaussian case. While counts in the lower-mass range in the Gaussian case are higher by a factor of $\sim 30 - 40$ than the corresponding counts in the higher-mass range, here a mere factor of ~ 3 is seen. In case (b) the results are even more interesting, since the total counts are dominated by high-mass clusters, lying at $0 \lesssim z \lesssim 3.5$. The cumulative counts at the lowest redshifts consist of a slightly higher contribution from the high-mass range and are larger by a factor ~ 1.3 than the corresponding contribution from mass range $10^{14} h^{-1} M_\odot < M < 10^{15} h^{-1} M_\odot$. Differences in total counts are large; in the Gaussian model these are ~ 4000 and ~ 3000 in cases (a) and (b), respectively, as compared to levels of $\sim 30,000$ and $\sim 10,000$ in the corresponding cases of the χ_1^2 model.

Fig. 8 describes cumulative number counts for two more frequency channels, $\nu = 143$ GHz and $\nu = 545$ GHz, in addition to $\nu = 353$ GHz which was used above. In the non-relativistic electron velocity limit the (thermal component of

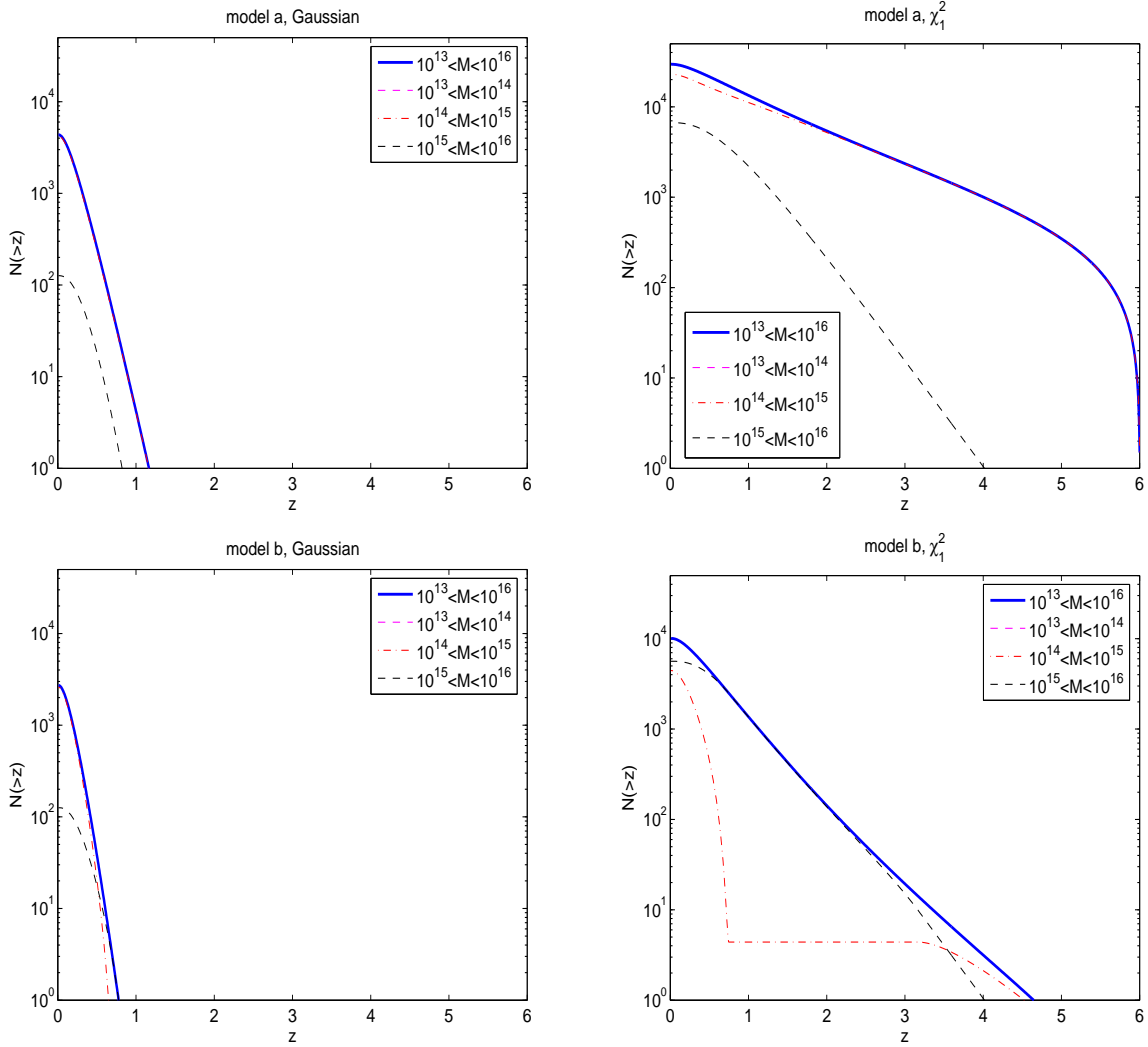


Figure 7. Cumulative S-Z counts as a function of redshift; shown are contributions from 4 mass intervals. Note that the contribution from the lowest mass interval ($10^{13} < M < 10^{14}$ solar masses) vanishes in all cases considered.

the) S-Z spectral function - which is essentially independent of the gas temperature - is $g(x)$ (eq. 19). At these frequencies, $g(x) = -4, 3.2, 6.7$, respectively, so our results for $\nu = 353$ GHz can be easily scaled accordingly. Adopting the same value of the limiting flux ($30mJy$), we find that values of the ratios of number counts at $\nu = 353$ GHz and $\nu = 545$ GHz are larger in the Gaussian than in the χ_1^2 model. This can clearly be attributed to the significantly higher population of clusters with flux exceeding the limit in the χ_1^2 model. Note that an accurate calculation of the S-Z intensity change necessitates a relativistic calculation (Rephaeli 1995) which yields a more complicated expression for the *temperature-dependent* spectral function (for which there are a few analytic approximations; see, e.g., Shimon & Rephaeli 2004, Itoh & Nozawa 2004). The deviation from the nonrelativistic calculation can amount to few tens of percent for typical temperatures in the range 5-10 keV. Since our main focus here is a comparison between predictions of the two density fields for quantities that are integrated over the cluster population (rather than an accurate description of the effect in a given cluster), it suffices to use the much simpler function $g(x)$.

We may summarize the results of this subsection as follows: total count levels are significantly higher in the χ_1^2 model, roughly by factors of ~ 7.5 and ~ 3 in cases (a) and (b), respectively. The Contribution of high-mass clusters to the total cumulative counts are practically negligible in the Gaussian case, but important in the non-Gaussian model, particularly so in case (b) where the lower-mass clusters fail to generate sufficient S-Z flux by virtue of their lower temperatures with respect to the evolving temperature scenario in case (a). In addition to this, the counts are more broadly distributed in redshift space in the non-Gaussian model due to the higher abundance of clusters at high redshifts.

As in the section describing the S-Z power spectrum, a comparison with published works on S-Z number counts is pertinent. Springel et al. (2001) find ~ 0.6 clusters per square degree for an observation frequency of $150 GHz$ and a flux

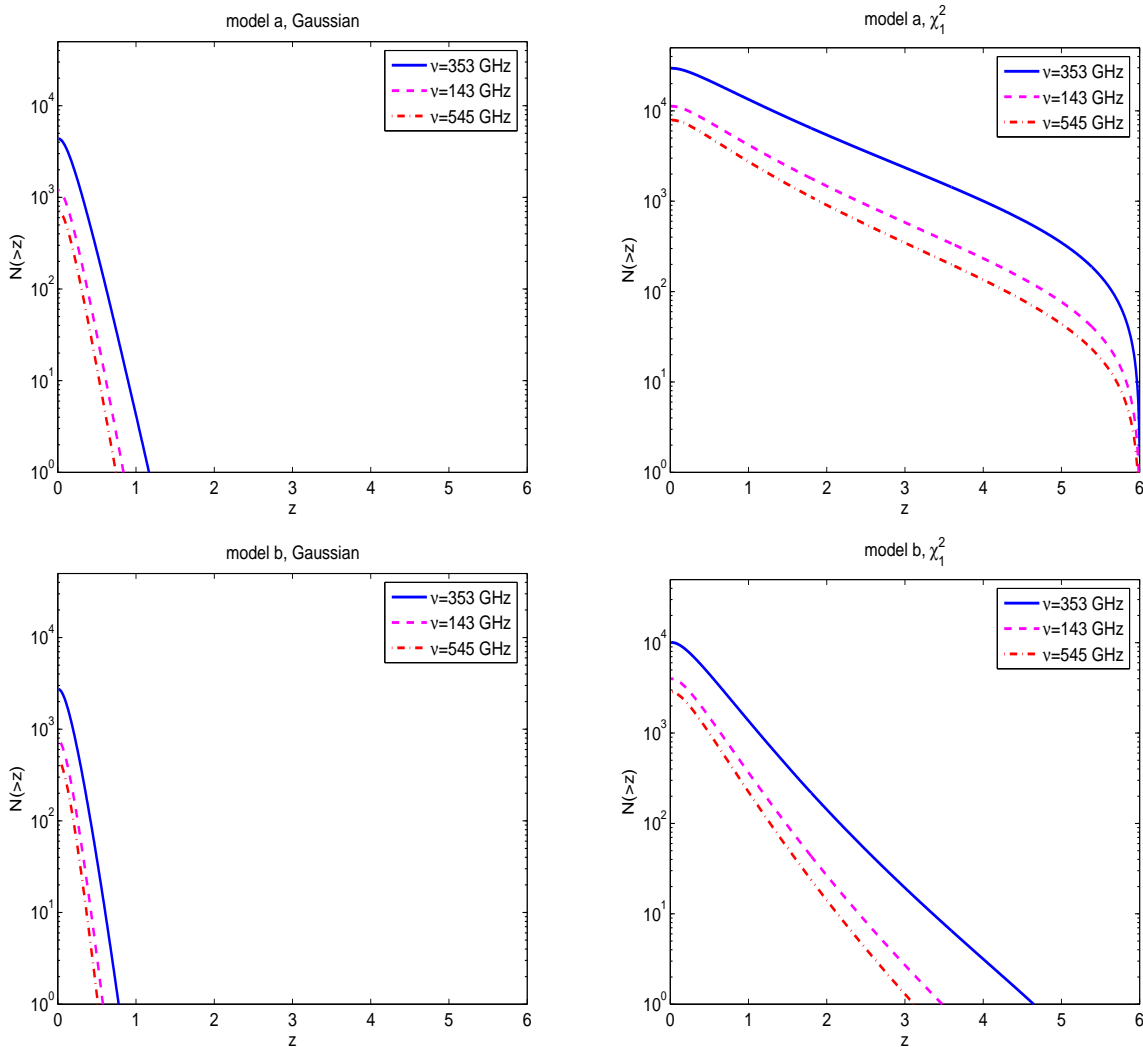


Figure 8. Cumulative S-Z counts as a function of redshift. Number counts are shown for the three specified frequency channels of the HFI instrument on the *Planck* satellite.

limit similar to ours, 30 mJy . This translates into all-sky counts of $\sim 2.5 \sim 10^4$ clusters, whereas we find $\sim 4 \cdot 10^3$. Holder et al. (2000) report a prediction of ~ 25 clusters per square degree, or a total of over 10^6 clusters. However, it is not clear what was the flux limit they assumed. In addition, the slightly higher normalization they adopted, $\sigma_8 = 1$, may be partly responsible for the inferred high counts. Benson, Reichardt & Kamionkowski (2002) find ~ 0.2 clusters per square degree for *PLANCK* specifics, with observation frequency 143 GHz and flux limit 30 mJy . An all-sky survey is then expected to yield ~ 8000 clusters. While our predictions are lower, it should be emphasized that similar to results for the S-Z power spectrum, S-Z cluster counts are equally susceptible to uncertainties in IC gas modeling and to the specifics of the experimental setting, such that a large scatter in the results is unavoidable. Moreover, our main concern in this study is the difference between the magnitudes of S-Z observables as predicted by two different mass functions, and those would certainly persist were we to modify the modeling of the IC gas and any other component relevant to the calculation of the effect.

3.3 A comparison between the χ_1^2 and χ_2^2 cases

It is useful to examine the sensitivity of the results corresponding to the χ_m^2 model to the number of fields added in quadratures, m . We have repeated the numerical calculations of the S-Z power spectrum and number counts (and in addition, the 2-point angular correlation function of S-Z clusters, which is dealt with separately in the next section) with $m = 2$ for case (a). Since the degree of skewness of the initial probability density function is reduced with increasing m , this will be manifested in the mass function as well, and necessitates a different normalization parameter σ_8 . For $m = 2$ it is found that in order to reproduce the observed cluster abundance at $z = 0$, $\sigma_8 = 0.77$, instead of the lower value of $\sigma_8 = 0.73$ in the $m = 1$ model.

Results of the calculations are illustrated in Fig. 9. The differences are quite significant in both plots; power levels in the

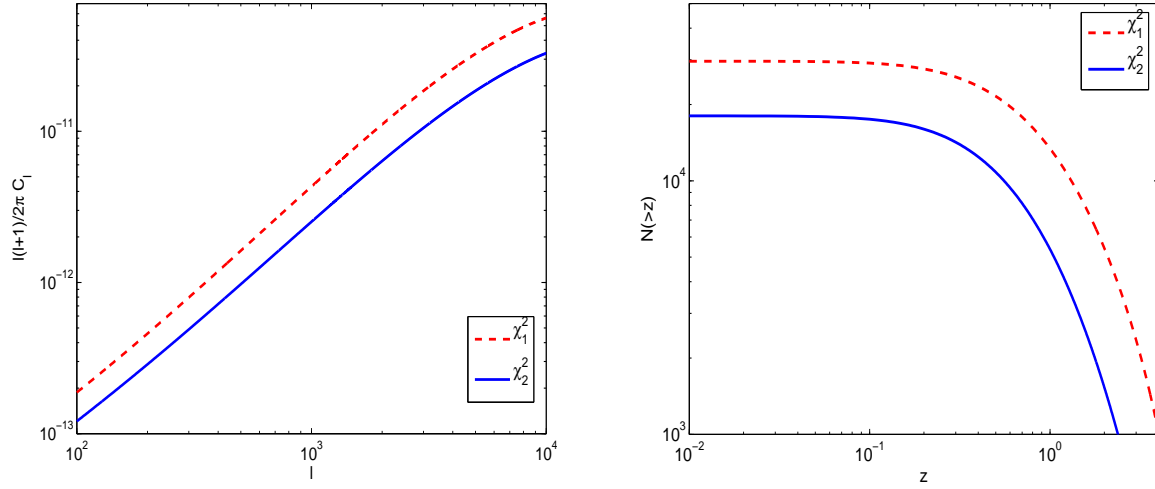


Figure 9. A comparison between S-Z power levels (left-hand panel) and number counts (right-hand panel) for a χ_m^2 -distributed density field with $m = 1$ and $m = 2$ is shown. Calculations were carried out for case (a).

$m = 1$ case are higher by a factor of $\sim 1.5 - 1.8$ across the multipole range of $100 \leq \ell \leq 10000$. It is the highest-mass clusters that are most susceptible to the high-mass tail of the mass function, which is strongly dependent on the parameter m . In particular, this is most noticeable at high redshifts where the predictions of the mass function for the massive clusters in the $m = 1$ and $m = 2$ cases vary greatly. Since these distant clusters have small angular sizes, it is not surprising that the ratio between the two curves increases with increasing multipole, reflecting the relative higher abundance of clusters with small apparent sizes for $m = 1$. This is further established by noting that the number counts ratio for $m = 1$ and $m = 2$ are highest at high redshifts: While the ratios are ~ 6 and ~ 3.5 at $z \sim 4$ and $z \sim 2$, respectively, the cumulative counts for $m = 1$ at $z = 0.1$ are approximately ~ 1.5 times as high as those obtained for $m = 2$. Clearly, very massive clusters at high redshifts are more common in the model with $m = 1$ than in that with $m = 2$.

4 ANGULAR CORRELATION FUNCTION OF S-Z CLUSTERS

The angular 2-point correlation function (hereafter A2PCF) is expected to be steeply dependent on the mass function, even more strongly than the angular power spectrum and cluster number counts, due to the *quadratic* dependence on the cluster abundance. The A2PCF of S-Z clusters has been studied by Diaferio et al. (2003), who explored the dependence of the expected number of cluster pairs on the biasing relation between the cluster and the mass distribution, and Mei & Bartlett (2003), who studied the feasibility of alleviating the degeneracy between Ω_m and σ_8 by means of combining S-Z cluster counts with their angular correlation function. The requisite data will become available when targeted S-Z cluster surveys are carried out. As pointed out by Mei & Bartlett, the scientific yield from the A2PCF lies in the fact that S-Z cluster catalogs, on their own, may constitute an important probe of cosmological models and cluster properties, even without the detailed follow-up observations of individual clusters. Here we calculate the A2PCF of S-Z clusters for the Gaussian and χ_1^2 mass functions and assess its diagnostic use to distinguish between the two models.

4.1 Formalism

The angular correlation function can be calculated by equating the surface density of S-Z clusters with their integrated spatial density:

$$\begin{aligned}
 d\Omega_1 d\Omega_2 \left[\int_z \int_M r^2(z) \frac{dr(z)}{dz} n(M, z) dz dM \right]^2 [1 + w(\theta)] &= d\Omega_1 d\Omega_2 \\
 \times \int_{z_1} \int_{z_2} \int_{M_1} \int_{M_2} r^2(z_1) \frac{dr(z_1)}{dz_1} r^2(z_2) \frac{dr(z_2)}{dz_2} n_1 n_2 [1 + \xi(M_1, M_2, z_1, z_2, R)] & dz_1 dz_2 dM_1 dM_2,
 \end{aligned} \tag{22}$$

where $\xi(M_1, M_2, z_1, z_2, R)$ is the spatial 2-point correlation function of clusters with masses M_1 and M_2 , located at redshifts z_1 and z_2 , and separated by physical distance R , and $n_i \equiv n(M_i, z_i)$. As in the calculation of the number counts, the lower limits of the integrals are set so as to yield S-Z fluxes that exceed the detection limit. Since the uncorrelated surface density

term on the left-hand side of equation (22) is identical with the integrated spatial density of the uncorrelated term on the right-hand side, the angular correlation function can be evaluated as

$$w(\theta) = \frac{\int_{z_1} \int_{z_2} \int_{M_1} \int_{M_2} r^2(z_1) \frac{dr(z_1)}{dz_1} r^2(z_2) \frac{dr(z_2)}{dz_2} n_1 n_2 \xi(M_1, M_2, z_1, z_2, R) dz_1 dz_2 dM_1 dM_2}{\left[\int_z \int_M r^2(z) \frac{dr(z)}{dz} n(M, z) dz dM \right]^2}. \quad (23)$$

It remains to specify the spatial correlation function of clusters, ξ . This can be done either by employing the observational correlation function of clusters (e.g. Bahcall & Soneira 1983), or by regarding it as the biased counterpart of the correlation function of dark matter, ξ_{dm} . We choose to employ the second method, in which the cluster correlation function is commonly written as

$$\xi(M_1, M_2, z_1, z_2, R) = b(M_1, z_1) b(M_2, z_2) \xi_{dm}(R, z), \quad (24)$$

where b is the linear bias factor. Making use of the global isotropy of the universe, we can express the correlation function as the Fourier-transformed power spectrum of dark matter:

$$\xi_{dm}(R, z) = \int \int \int e^{i\vec{k} \cdot \vec{R}} P(\vec{k}) d^3\vec{k} = \frac{A}{2\pi^2} \int_0^\infty k^{n+2} T^2(k) \frac{\sin kR}{kR} dk. \quad (25)$$

The simplest form for the bias factor is (Matarrese et al. 1997, Catelan et al. 1998)

$$b(M, z) = 1 + \frac{\delta_c}{\sigma_M^2(z)} - \frac{1}{\delta_c}. \quad (26)$$

Note that more accurate formulae for the bias factor exist, which take into account non-spherical collapse (Sheth, Mo & Tormen 2001) and nonlinear clustering effects (Peacock & Dodds 1996); we will limit ourselves here to the simplest case, since our main objective in this study is a comparative evaluation of the predictions of two mass functions (rather than their respective accuracy).

To proceed, it is necessary to write down the physical distance R between the members of a cluster pair, separated by an angle θ . In doing so it is very convenient to take advantage of the fact that the observational spatial correlation function falls off rapidly with distance, $\xi(R) \sim R^{-1.8}$ (e.g. Bahcall & Soneira 1983); a corresponding trend can be inferred from equation (25), although in this case it is obviously different from a power law. Consequently, correlated clusters must lie at low angular separations and at approximately the same redshift. The separation can be written as

$$R = \sqrt{[r(z_1) - r(z_2)]^2 + (d_A \theta)^2}, \quad (27)$$

where r and d_A denote the radial and angular diameter distance, respectively. Substituting $z \equiv (z_1 + z_2)/2$ and $u \equiv z_1 - z_2 \ll 1$ yields

$$r(z_1) - r(z_2) = r(z_2 + u) - r(z_2) \approx r(z_2) + \frac{dr}{dz}(z_2) \cdot u - r(z_2) \approx u \cdot \frac{dr}{dz}, \quad (28)$$

and the separation simply becomes

$$R = \sqrt{\left[u \cdot \frac{dr}{dz} \right]^2 + [d_A(z) \cdot \theta]^2}. \quad (29)$$

Substituting this in the numerator of equation (23), together with the spatial correlation function of equation (24), we have

$$r^2(z_1) \frac{dr(z_1)}{dz_1} r^2(z_2) \frac{dr(z_2)}{dz_2} \approx r^4(z) \left(\frac{dr}{dz} \right)^2 du dz, \quad (30)$$

so that we can now write

$$w(\theta) = \int_z \int_{M_1} \int_{M_2} r^4(z) \left[\frac{dr(z)}{dz} \right]^2 n(M_1, z) n(M_2, z) b_1(M_1, z) b_2(M_2, z) dM_1 dM_2 dz \\ \times \int_{-\infty}^\infty \xi \left[\sqrt{\left[\frac{dr}{dz} \cdot u \right]^2 + [d_A(z) \cdot \theta]^2}, z \right] du \times \left[\int_z \int_M r^2(z) \frac{dr(z)}{dz} n(M, z) dz dM \right]^{-2}. \quad (31)$$

The integration over the spatial correlation function may be performed by substituting the cluster separation R (equation 29) in the dark matter correlation equation (25), which is in turn substituted in the integral over u in equation (31):

$$\frac{A}{2\pi^2} \int_0^\infty k^{n+2} T^2(k) dk \int_{-\infty}^\infty \frac{\sin k \sqrt{\left[\frac{dr}{dz} \cdot u \right]^2 + [d_A(z) \cdot \theta]^2}}{k \sqrt{\left[\frac{dr}{dz} \cdot u \right]^2 + [d_A(z) \cdot \theta]^2}} du, \quad (32)$$

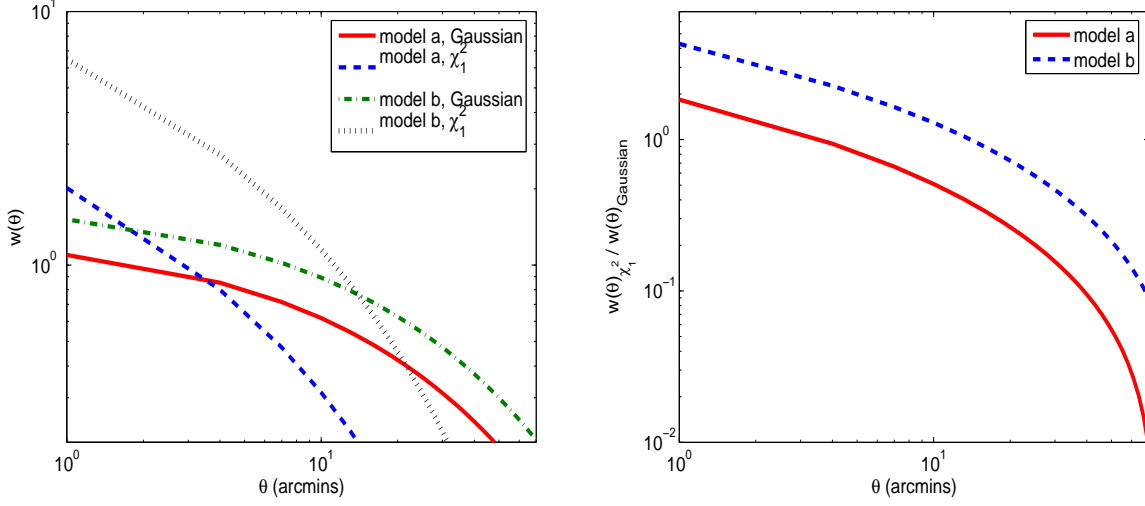


Figure 10. The A2PCF calculated for the Gaussian and χ_1^2 models for cases (a) and (b). The left-hand panel describes the correlation levels, whereas the right-hand panel depicts the ratios between the χ_1^2 and Gaussian models.

where the last expression was obtained by changing the order of integration. The integral over u can be performed using the following change of variables:

$$x \equiv \frac{\sqrt{\left(\frac{dr}{dz} \cdot u\right)^2 + (d_A(z) \cdot \theta)^2}}{d_A(z) \cdot \theta}, \quad (33)$$

which results in an integral that can be put in a closed form

$$\frac{2}{k(dr/dz)} \int_1^\infty \frac{\sin[kx d_A(z)\theta] dx}{\sqrt{x^2 - 1}} = \frac{\pi}{k(dr/dz)} J_0[kd_A(z)\theta], \quad (34)$$

where x was defined above and J_0 is a Bessel function of the first kind and order zero. Expression (32) then finally becomes

$$\frac{A}{2\pi(dr/dz)} \int_0^\infty k^{n+1} T^2(k) J_0[kd_A(z)\theta] dk. \quad (35)$$

This integral can be easily evaluated numerically.

4.2 Results

The A2PCFs in cases (a) and (b) in the Gaussian and χ_1^2 models are plotted in Fig. 10. Their shapes are dictated by the functional form of the spatial correlation function, which is dominated by the Bessel function of the first kind and order zero appearing in equation (35). Referring first to the differences between the predictions of cases (a) and (b), it can be seen that in both the Gaussian and χ_1^2 models the correlation levels are higher in case (b). The reason for this is easily explainable noting that case (b) is biased towards higher-mass clusters owing to its lack of temperature evolution; as clusters do not become hotter with increasing redshift as in case (a), only very massive clusters generate detectable S-Z signals. These higher-mass clusters are more strongly correlated, as indicated by the bias term, equation (26), by virtue of its specific dependence on the mass variance $\sigma(M)$, a monotonically decreasing function of mass M . Thus, the bias factor is a monotonically increasing function of M , giving rise to stronger correlations among high-mass cluster populations.

In order to explain the differences between the predictions of the χ_1^2 and Gaussian models in either case (a) or (b), it will first be useful to give a qualitative explanation of the shape of the A2PCF curve. We may think of an effective maximum physical separation for which (positive) correlation between two clusters is still possible. At low angular separations the scale corresponding to this limiting distance can be subtended at relatively high redshifts, so contribution to the A2PCF at this angle is possible from low as well as high redshifts. With increasing angular separation the corresponding scale can only be subtended at lower redshifts, so that the main contribution to the correlation is generated locally. Since the χ_1^2 model yields higher cluster populations (and particularly so of high-mass clusters) at high redshifts, it is natural to expect higher correlation levels than in the corresponding Gaussian case, where the cluster population is limited to lower redshifts, and also relatively limited in massive clusters. As can be seen in the right-hand panel of Fig. 10 at angular separations of $\theta \gtrsim 3'$ and $\theta \gtrsim 10.5'$ in cases (a) and (b), respectively, the correlation levels in the χ_1^2 model fall below those of the Gaussian model. Since the redshift range available for contributing to the angular correlation function reduces with increasing angular

separation, this trend is indicative of a diminished contribution of relatively low-redshift clusters in the χ_1^2 model. In fact, this is indeed the case, and can be easily realized by inspection of the upper and lower-right hand panels of Figs. 1 and (7), where it has been shown that a substantial contribution to the power spectrum levels at high multipoles and to the cumulative number counts originates in clusters lying at high redshifts ($z > 1$). As explained above, at such high redshifts clusters are not strongly correlated at high angular separations by virtue of their mutual large physical distances. On the other hand, in the Gaussian model the corresponding contribution comes almost exclusively from low-redshift clusters, which may manifest relatively strong correlations even at higher angular separations. Clearly, this effect is also responsible for the steeper shape of the A2PCF curve in the non-Gaussian models.

5 DISCUSSION AND CONCLUSION

The main objective of this study has been to compare predictions of S-Z observables for two mass functions which differ mainly at the high mass end. A χ_1^2 distributed density fluctuation field is characterized by a longer tail of high density fluctuations with respect to the Gaussian case, and is capable of generating more high-mass clusters at higher redshifts, owing to the denser population of high density fluctuations (or peaks) which can collapse at earlier times. S-Z power spectrum, number counts, and 2-point angular correlation function all prove to yield significantly different results if calculated using a mass function derived from a Gaussian or χ_1^2 primordial density field. We have demonstrated that levels of the power spectrum in the latter model are higher by about an order of magnitude than in the former model, depending on the IC temperature scaling with the cluster mass. This was explicitly shown to take effect in light of the larger contribution of high-mass clusters and high redshift clusters to the total power in the non-Gaussian model. The larger contribution from distant clusters is also responsible for the higher multipoles at peak power.

We have shown that S-Z power spectrum levels are contributed by different cluster populations in the Gaussian and χ_1^2 models; in the former model, most of the power originates in clusters lying at $0 < z < 1$, with the exception of the higher multipoles for which a non-negligible amount of power comes from $1 < z < 2$. In contrast, in the latter model more power is contributed from higher redshift clusters, beginning at multipole ~ 3000 . On the other hand, most of the power is contributed by clusters lying in the mass range $10^{14} < M < 10^{15} M_\odot$. This holds for both models in the interesting multipole ranges.

The power spectrum is quite sensitive also to cluster internal properties, as is demonstrated in part through the modification of the cluster temperature scaling with mass, and by the dependence on the cluster core radius. These reflect the uncertainty of the actual scalings due to observational scatter, lack of high-redshift cluster data, and insufficient theoretical information. Plausible scatter of 10 – 20% in these scalings results in significant differences in levels of power, albeit to a considerably lower degree than those produced by replacing the Gaussian mass function with the χ_1^2 mass function. Number counts are also significantly higher in the χ_1^2 model (up to an order of magnitude), reflecting the higher population of high-redshift, massive clusters, capable of generating sufficient S-Z flux to be detected by upcoming experiments. These results obviously depend on the flux detection limit of the experiment, and are likely to become more pronounced with increasing limiting flux, owing to the high-mass cluster bias.

The 2-point angular correlation function of S-Z clusters is potentially an additional observable for which the Gaussian and χ_1^2 models may result in substantially different predictions. Depending on the temperature scaling with redshift, it has been shown that the correlation level at the lowest angular separations ($\sim 1'$) is higher by a factor ~ 2 and ~ 4 in the χ_1^2 model. On the other hand, at larger angular separations correlation levels are higher in the Gaussian model. This characteristic behaviour leads to a steeper functional form in the χ_1^2 model. Although not explicitly demonstrated in this study, the flux limit of the experiment is, of course, a major factor in determining the correlation levels, due to the fact that higher flux limits are biased towards more massive clusters, whose bias parameters are larger.

An additional relevant property which may be manifested differently in Gaussian and non-Gaussian density fields is cluster (or halo) formation time. Clusters are likely to form earlier in (positively skewed) non-Gaussian fields owing to the higher probability of finding an overdensity exceeding the critical density for collapse with respect to the corresponding probability in a Gaussian density field. This may bear consequences for, e.g., the concentration parameter of haloes, a key parameter of the NFW dark matter profile (Navarro, Frenk & White 1995). The concentration parameter is expected to assume higher values with earlier formation time by virtue of the higher background density. In this context the recent result from a lensing analysis of the cluster A1689 (Broadhurst et al. 2005) is of particular interest. A very steep mass profile was deduced in this analysis, one that is fit by an extremely high concentration parameter of $c = 13.7_{-1.1}^{+1.4}$. This value seems to be at a considerable variance with theoretical predictions. Observations of two other clusters yield $c \sim 12$ for MS 2137-23 (Gavazzi et al. 2003), and $c \simeq 22$ and $c \simeq 4$ for the main and secondary clumps in the cluster C1 0024 (Kneib et al. 2003). Although perhaps not very meaningful from a statistical point of view, these results may be indicative of earlier formation times, which are favoured in positively-skewed non-Gaussian fields.

The temperature of the IC gas of virialized clusters may also be affected by the cluster formation time. In conventional temperature-mass relations it is the observed redshift of a cluster that determines its temperature. In this *recent formation*

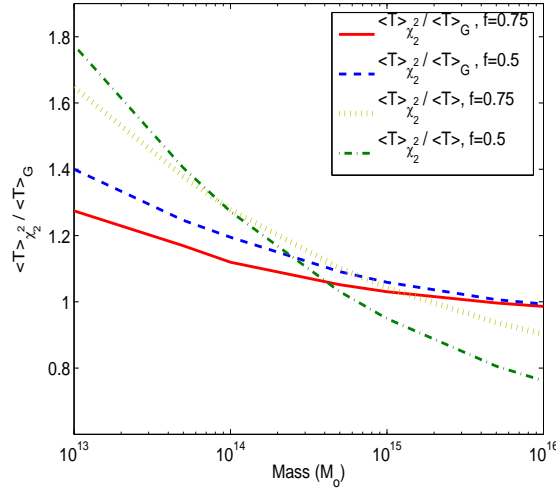


Figure 11. Ratios of effective temperatures are shown. The average temperature predicted in the χ_2^2 model is divided by the corresponding quantity in the Gaussian model for $f = 0.5$ and $f = 0.75$. Also shown is the ratio between the effective temperature in the non-Gaussian model and the temperature predicted by the temperature-mass relation provided in equation (13).

approach, the relevant redshift is the observation redshift. Clearly, this picture does not address the merging process that gives rise to the clusters we observe today. In the merger picture the formation redshift, z_f , may differ significantly from the cluster observed redshift, z_{obs} , and the predicted temperatures will vary accordingly.

The temperature and concentration parameter dependence on formation time are likely to influence S-Z observables; higher IC gas temperatures (stemming from earlier formation times) may give rise to an intensification of the effect, whereas, if one assumes that IC gas approximately traces the dark matter distribution, higher concentration parameters may bring about transfer of power to higher multipoles, in light of the resulting steeper gas density profile.

We have conducted a preliminary study of the probability distribution function (PDF) of formation times within the framework of Gaussian and χ_2^2 density fields. This initial work is based on the excursion set formalism and its derivatives (Bond et al. 1991, Lacey & Cole 1993). We note that the definition of the formation time used here is somewhat arbitrary; clusters were assumed to have formed once they assembled a fraction of either $f = 0.5$ or $f = 0.75$ of their current masses. We have found that on most relevant mass scales clusters form at higher redshifts in the χ_2^2 model. Defining “effective” cluster temperatures and concentration parameters by averaging these two quantities at specified formation redshifts over the PDF of formation times, we learn that temperatures and concentration parameters are on average higher in the χ_2^2 model for masses $10^{13} - 10^{15} M_\odot$. At higher masses the differences are practically negligible. Also, with increasing observation redshift, the differences become gradually less pronounced. This is related to the fact that the time range available for formation is reduced with increasing observation time, since the cluster must have formed at a redshift exceeding the observation redshift.

As an example of our preliminary results we include Fig. (11), which compares the effective IC gas temperature (as defined above) in the χ_2^2 and Gaussian models as a function of cluster mass, for $f = 0.75$ and $f = 0.5$. Also shown are the respective temperature ratios between the χ_2^2 predictions and those given by equation (13). Clearly, the indicated average temperatures are closely related to the redshift range at which the formation time PDF attains the highest levels. For example, the PDFs of the lowest mass scale ($10^{13} M_\odot$) peak at relatively high redshifts, and therefore the weight of the contribution from the $(1+z)$ factor is rather large. This results in higher average temperatures. The effect is most pronounced when comparing the χ_2^2 model with the non-averaged temperature of equation (13), since for the latter case all clusters are assumed to have formed at $z_{obs} = 0$. Obviously, $f = 0.5$ implies earlier formation times and higher average temperatures for a given (low) cluster mass. This holds also for the χ_2^2 model, which involves earlier formation times for this mass range. The average temperature predictions in the χ_2^2 and Gaussian models show that clusters of $10^{13} M_\odot$ are hotter by factors ~ 1.4 and ~ 1.27 for $f = 0.5$ and $f = 0.75$, respectively. For $M = 10^{14} M_\odot$ the corresponding factors are ~ 1.23 and ~ 1.12 , while for $M = 10^{15} M_\odot$ in both cases the factors are ~ 1 .

We may therefore conclude as follows: a mass function based on a χ_m^2 density fluctuation field gives rise to higher populations of massive clusters at relatively high redshifts with respect to a mass function derived on the basis of Gaussian density fluctuation fields. This generates higher levels of S-Z power spectrum and number counts by up to an order of magnitude. The 2-point angular correlation function of S-Z clusters is also susceptible to the mass function model and predicts higher correlations at low angular separations in the non-Gaussian model. At higher angular separations the correlation levels in a Gaussian field dominate. Cluster formation times are generally earlier in the non-Gaussian model, and may also give

rise to higher temperatures and concentration parameters of low-mass clusters observed at relatively low redshifts. A more rigorous exposition of the topic of formation times, their relevance to S-Z observables, and further related ramifications will be discussed in a future paper.

6 ACKNOWLEDGMENT

Work at Tel Aviv University is supported by a grant from the Israel Science Foundation. J.S. gratefully acknowledges support as a Visiting Sackler Scholar at the Institute of Advanced Studies, Tel Aviv University.

7 REFERENCES

- Bahcall N.A., Soneira R.M., 1983, *ApJ* , 272, 627
Bardeen J.M., Bond J.R., Kaiser N., Szalay A.S., 1986, *ApJ* , 304,15
Benson A.J., Reichardt C., Kamionkowski M., 2002, *MNRAS* , 331, 71
Bond J.R., Cole S., Efstathiou G., Kaiser N., 1991, *ApJ* , 379, 440
Bond J.R. et al., 2005, *ApJ* , 626, 12
Broadhurst T., Takada M., Umetsu K., Kong X., Arimoto N., Chiba M., Futamase T., 2005, *ApJ* , 619, L143-L146
Carlstrom, J.E., Holder, G.P., Reese, E.D. 2002, *ARA&A* , 40, 643
Carroll S.M., Press W.H., Turner E.L., 1992, *ARA&A* , 30, 499
Catelan P., Lucchin F., Matarrese S., Porciani C., 1998, *MNRAS* , 297, 692
Colafrancesco S., Mazzotta P., Rephaeli Y., Vittorio N., 1997, *ApJ* , 479, 1
Da Silva A.C., Kay S.T., Liddle A.R., Thomas P.A., Pearce F.R., Barbosa D., 2001, *ApJ* 561, L15-L18
Diaferio A., Nusser A., Yoshida N., Sunyaev R.A., 2003, *MNRAS* , 338,433
Gavazzi R., Fort B., Mellier Y., Pelló R., Daniel-Fort M., 2003, *A&A* , 403, 11
Holder G.P., Mohr J.J., Carlstrom J.E., Evrard A.E., Leitch E.M., 2000, *ApJ* , 544, 629
Itoh N., Nozawa S., 2004, *A&A* , 417, 827
Kneib J.P. et al., 2003, *ApJ* , 598, 804
Komatsu E. et al., 2003, *ApJS* , 149, 119
Koyama K., Soda J., Taruya A., 1999, *MNRAS* , 310, 1111
Kuo C.L. et al., 2004, *ApJ* , 600, 32
Kurk J., Venemans B., Röttgering H., Miley G., Pentericci L., 2004, in Plionis M., ed., *Multiwavelength Cosmology*. Kluwer, Dordrecht, preprint (astro-ph/0309675)
Lacey C., Cole S., 1993, *MNRAS* , 262, 627
Mason B., Pearson T.J., Readhead A.C.S., Sheperd M.C., Sievers J.L., Udomprasert P.S., Cartwright J.K., Farmer A.J., et al., 2003, *ApJ* , 591, 540
Matarrese S., Coles P., Lucchin F., Moscardini L., 1997, *MNRAS* , 286, 115
Mathis H., Diego J.M., Silk, J., 2004, *MNRAS* , 353, 681
Mei S., Bartlett J.G., 2003, *A&A* , 410, 767
Miley G.K. et al., 2004, *Nat* , 427, 47
Molnar S.M., Birkinshaw M., 2000, *ApJ* , 537, 542
Mullis C.R. et al., 2003, *ApJ* 594, 154
Navarro J.F., Frenk C.A., White S.D.M., 1995, *MNRAS* , 275, 720
Norman, M.L. 2005, preprint (astro-ph/0511545)
Peacock J.A., Dodds S.J., 1996, *MNRAS* , 280, 19
Press W.H., Schechter P., 1974, *ApJ* , 187, 425
Refregier A., Teyssier R., 2002, *Phys. Rev. D*, 66, 043002
Rephaeli Y., 1995, *ARA&A* , 33, 541
Sheth R.K., Mo H.J., Tormen G., 2001, *MNRAS* , 323, 1
Shimon M., Rephaeli Y., 2004, *NewA* , 9, 69
Springel V., White M., Hernquist L., 2001, *ApJ* , 549, 681
Vikhlinin A., McNamara B.R., Forman W., Jones C., Quintana J., Hornstrup A., 1998, *ApJ* , 498, L21